

Haptic Transparency and Interaction Force Control for a Lower-Limb Exoskeleton

Emek Barış Küçüktabak^{1,2,3}, Yue Wen^{3,4}, Sangjoon J. Kim^{3,4}, Matthew Short^{3,5}, Daniel Ludvig⁵,
Levi Hargrove^{2,3,4}, Eric Perreault^{2,3,4,5}, Kevin Lynch^{1,2}, and Jose Pons^{1,2,3,4,5}

Abstract—Controlling the interaction forces and torques between a human and an exoskeleton is crucial for adjusting assistance or resistance levels while allowing voluntary motion in daily life or clinical settings. It is an open problem, however, to control the interaction forces of lower-limb exoskeletons designed for unrestricted overground walking, i.e., floating base exoskeletons with feet that contact the ground. For these types of exoskeletons, it is challenging to measure interaction forces as it is not feasible to implement force/torque sensors at every contact between the user and the exoskeleton. Moreover, it is important to compensate for the exoskeleton’s whole-body gravitational and dynamical forces. Previous works either simplified the dynamic model by treating the legs as independent double pendulums, or they did not close the loop with interaction force feedback.

This paper presents a novel method to calculate interaction torques during the complete gait cycle by using whole-body dynamics and joint torque measurements on a hip-knee exoskeleton. Furthermore, we propose a constrained optimization scheme combined with a virtual model controller to track desired interaction torques in a closed loop while considering physical limits and safety considerations. Together, we call this approach whole-exoskeleton closed-loop compensation (WECC) control. We evaluated the haptic transparency and spring-damper rendering performance of WECC control on three subjects. We also compared the performance of WECC with a controller based on a simplified dynamic model and a passive version of the exoskeleton with disassembled drives. The WECC controller resulted in consistent interaction torque tracking during the whole gait cycle for both zero and nonzero desired interaction torques. On the contrary, the simplified controller failed to track desired interaction torques during the stance phase. The proposed interaction force control method is especially beneficial for heavy lower-limb exoskeletons where the dynamics of the entire exoskeleton should be compensated.

Index Terms—Physical human-robot interaction, exoskeletons, interaction force control, rehabilitation robots, assistive robots

I. INTRODUCTION

Lower-limb exoskeletons are used to assist impaired individuals in their daily life and as a tool for physical rehabilitation in clinical settings [1], [2]. They are also increasingly used

to augment the abilities of healthy individuals [3]. In each of these applications, the exoskeleton must be capable of regulating the interaction forces and torques between the user and the exoskeleton, both for the safety of the user and the effectiveness of the control mode.

As an example, the *transparent* control mode attempts to zero the interaction forces between the user and the exoskeleton. Transparency is useful for comparison when evaluating new rehabilitation control strategies [4] and for allowing users to move freely when wearing assistive devices [5]. Other control modes, used in rehabilitation, include “assist as needed” (AAN) and resistive control for robot-aided gait therapy [6]. With AAN, the robot provides only as much assistance force as needed to complete a given task [7]. In resistive and error-augmentation methods, force is applied to make the task more challenging, which accelerates the relearning of motor tasks [4], [8].

An important part of controlling interaction forces is compensating the weight of the lower-limb exoskeleton. How the weight of the exoskeleton is transferred to the ground or the user depends on its design. There are three main categories of design:

a) *Grounded trunk*: The trunk of the exoskeleton is fixed relative to a treadmill structure [9]–[11]. Due to the grounded trunk, only the masses of the individual leg links are felt by the user, and these masses can be compensated with active control.

b) *Floating base (trunk) without feet*: These exoskeletons are designed for unrestricted overground walking and do not contact the ground [12]–[14]. Partial gravity compensation can be achieved for the swing leg, but it is not possible for the robot to completely carry its own weight since there is no contact with the ground. Such exoskeletons are designed to be as light as possible, which limits their maximum assistance/resistance and battery life.

c) *Floating base with feet*: These exoskeletons are designed for unrestricted overground walking and have feet that contact the ground [15]–[21]. The weight of the exoskeleton can be transferred to the ground through the exoskeleton’s foot contact. While this allows for stronger actuators and larger batteries, it comes at the cost of more complicated controllers or diminished haptic transparency.

In this paper we focus on floating base lower-limb exoskeletons with feet, for which controlling interaction forces remains an open problem [22]. Solving this challenging problem will allow more natural overground therapy by rehabilitation robots and larger assistive forces by assistive devices.

This work was supported by National Science Foundation / National Robotics Initiative (Grant No: 2024488), Northwestern University and the Turkish Fulbright Commission

¹ Department of Mechanical Engineering, McCormick School of Engineering, Northwestern University, Evanston, IL, USA

² Center for Robotics and Biosystems, Evanston, IL, USA

³ Shirley Ryan AbilityLab, Chicago, IL USA

⁴ Department of Physical Medicine and Rehabilitation, Feinberg School of Medicine, Northwestern University, Chicago, IL, USA

⁵ Department of Biomedical Engineering, Northwestern University, Evanston, IL, USA

Due to the high torque requirements of floating base exoskeletons with feet, high reduction ratios are used, which results in high friction and apparent inertia of motor rotors [23]. Also, these exoskeletons are heavy due to powerful actuators and large batteries. Therefore, it is essential to compensate for these factors to accurately control the interaction forces and torques between the user and the robot.

Another challenge is measuring the interaction torques between the human and the exoskeleton. Grounded exoskeletons typically have a small number of contacts with the user, and interaction forces can be directly measured by force sensors implemented at the contacts [10], [24], [25]. In contrast, floating base exoskeletons have broadly distributed contact with the user, including at the trunk and foot. This makes it impractical to implement force/torque sensors at all contacts. Therefore, it is required to indirectly estimate the interaction forces and torques through other sensory information.

In this paper, we present a novel whole-exoskeleton closed-loop compensation (WECC) controller to estimate and control user-exoskeleton interaction torques during the complete gait cycle of a floating-base hip-knee exoskeleton with feet. The controller, which is based on constrained optimization, outperforms the state of the art in achieving transparency (zero impedance) and nonzero impedances in the user-exoskeleton interaction behavior.

The context of the contribution of this paper is established by the related work below.

A. Related Work

Previous studies on controlling interaction forces with floating base lower-limb exoskeletons with feet can be divided into three main categories.

1) *Whole-body dynamics compensation with no interaction force feedback:* A lower-limb exoskeleton can be modeled as a floating base system considering all links and joints together, similar to a bipedal robot [26], [27]. While bipedal robots are only in contact with the ground, lower-limb exoskeletons are also in contact with the user through multiple connection points.

Vantilt et al. [16] implemented a whole-body floating base model while considering external contact constraints such as ground contact or contact with a stool. They estimated the contact forces based on a complementary energy method [28] using the stiffness values of the exoskeleton parts together. However, this method does not allow the calculation of interaction torques between the human and robot, as the contact points between the human and exoskeleton are not static. Camardella et al. [15] similarly modeled the full-body dynamics but constituted the equation of motion based only on a model of a single foot in contact with the ground. Even though only left and right stance models were used, they interpolated the dynamics during double stance between left and right stance models based on a user-dependent continuous gait state estimation.

These studies compensated for the gravitational and Coriolis torques calculated using the whole-body model. However, modeling errors were not corrected with interaction force

feedback, and desired interaction torques were used only as a feedforward term. The use of series elastic actuation [16], [28] or torque motors with tendon-based transmission [15] results in low friction and high joint torque control capabilities, which reduces modeling errors. However, these solutions are not typically used in commercially-available devices like the ExoMotus-X2 exoskeleton studied in this paper.

2) *Simplified double pendulum model with interaction force feedback:* Andrade et al. [17], [18], and Tue et al. [19] employ a simpler, non-whole-body model of the exoskeleton to help estimate interaction torques. In this simplified model, each leg is modeled as an independent double pendulum 2R robot. When the leg is swinging, the hip joint is assumed to be fixed. When the leg is in contact with the ground, the ankle joint is assumed to be pinned. This model is used to calculate the feedforward compensation torques, which consist of inertial, gravitational, and Coriolis forces. These terms are subtracted from the joint torque measurements to estimate the interaction torques between the human and exoskeleton. Interaction torque estimation is used as the input of a proportional-derivative (PD) or admittance controller.

Since the backpack is not modeled and the legs are modeled independently, the dynamic compensation torques and interaction torque estimates are not accurate for the stance leg. With this approach, the stance leg carries only its own weight instead of the weight of the entire exoskeleton. While this might be acceptable for light or grounded exoskeletons, it is not accurate for exoskeletons designed for overground walking that provide a high level of support and long battery life.

3) *User-dependent or user-instrumented approaches:* Since physical parameters and walking gaits vary from user to user, some interaction force controllers require additional sensors to be affixed to the user and/or custom tuning for each user.

Sharifi et al. [20] implemented a neural network scheme to learn the whole-body dynamics of the exoskeleton together with the user. In the learning phase, the user is asked to relax while the exoskeleton applies predefined torque patterns. The learned passive dynamics are subtracted from the actual motor torques to estimate the human-robot interaction torque. Because the dynamics are learned based on the motor torque recordings, frictional effects are included in the model. Therefore, this method does not require additional sensors to measure the joint torques, and motor current measurements are enough. On the other hand, the main drawback of this method is that the learned dynamics is user-dependent, and a training phase is required for each user.

Kazerooni et al. [21] implemented a hybrid controller where the exoskeleton's stance leg follows the joint positions of the user to provide haptic transparency. The joint positions of the user's leg are measured by inclinometers attached to it. For the swing leg, a sensitivity amplification controller was implemented, which compensates for the dynamics of the swing leg and reacts to the disturbances applied by the user to minimize the interaction torques. One drawback of this method is the required additional instrumentation on the user that increases the time to don and doff the exoskeleton. Moreover, if it is required to provide nonzero desired interaction torques, this would require a model of the user-dependent interaction

TABLE I: Selected features of the interaction force/torque control studies. Note that this paper focuses on floating-base lower-limb exoskeletons with feet. Therefore, this table does not include studies with grounded exoskeletons and floating-base lower-limb exoskeletons without feet.

Reference	Model	Interaction force feedback	User dependent	Instrumentation on user	Physical/safety limit implementation
Camardella et al., 2021 [15]	Whole-body	No	Yes	No	No
Vantilt et al., 2019 [16]	Whole-body	No	No	No	No
Andrade et al., 2019-21 [17], [18]	Independent double pendulums	PD controller	No	No	No
Tu et al., 2020 [19]	Independent double pendulums	Admittance controller	No	No	No
Sharifi et al., 2021 [20]	Whole-body (learnt by NN)	No	Yes	No	No
Kazerooni et al., 2006 [21]	3-link for swing no model for stance (position control)	Sensitivity Amplification	No (transparency) Yes (non-zero reference)	Yes	No
Our proposed method (WECC)	Whole-body	Admittance controller	No	No	Yes

properties to calculate desired joint positions of the stance leg.

4) *Summary*: Selected features of interaction force/torque control studies on floating base lower-limb exoskeletons that contact the ground are presented in Table I. These studies can be categorized into three main groups. First, there are studies where the whole-body dynamics of the exoskeleton are compensated with no interaction force feedback [15], [16], [20]. Second, some studies modeled the exoskeleton as two independent legs with no consideration of the backpack [17]–[19]. These studies implemented PD or admittance controllers based on the interaction force/torque error. Third, there are methods that require additional instrumentation on the user [21] or user-dependent learning for model or gait state estimation [15], [20]. None of the proposed control methods considers actuation limits or other safety requirements such as velocity limits.

To the best of our knowledge, there is no study that calculates interaction forces with full body dynamics during the whole gait cycle and uses this estimation in a closed-loop control for a floating-base lower-limb exoskeleton that is in contact with the ground.

B. Contributions

In this paper, we propose a novel subject-independent method to calculate interaction forces during both single and double stance configurations based on a whole-body dynamic model. Moreover, we propose constrained optimization combined with a virtual model controller to achieve desired interaction torques while considering physical and safety constraints.

We evaluated the transparency and spring-damper haptic-rendering performance of our proposed whole-exoskeleton closed-loop compensation (WECC) controller on treadmill walking. We compared the performance of WECC controller to a control approach based on a simplified dynamic model of the exoskeleton, where the legs are modeled as double pendulums independent of one another and the backpack is ignored [17]–[19], [23]. For transparency evaluations, we also tested the performance of a passive version of the exoskeleton with disassembled drives.

We observed that the transparency of the swing leg was similar under the three conditions (WECC, Simplified, and No-drive), but our proposed WECC method outperformed the simplified controller and the no-drive condition for the stance leg. In nonzero impedance haptic rendering, WECC and simplified controllers performed similarly for the swing leg, but our WECC controller tracked the desired interaction torques better for the stance leg.

The core contributions of this article are as follows:

- 1) A continuous whole-body forward dynamical model for the whole gait cycle is developed based on the ratios of the vertical ground reaction forces at the feet.
- 2) A novel method to estimate the interaction forces during both single and double stance configurations is proposed.
- 3) A constrained-optimization-based virtual mass controller is implemented that considers the underactuation of the exoskeleton and its physical/safety constraints to control the interaction torques.
- 4) The transparency and haptic rendering performance of our proposed WECC controller is compared to a state-of-the-art controller based on a simplified dynamic model.

II. SYSTEM DESCRIPTION AND MODELING

A. Lower-limb Exoskeleton: X2

A four degrees-of-freedom (DoF) lower limb exoskeleton (ExoMotus-X2, Fourier Intelligence, Singapore), shown in Figure 1, was adapted and used as a platform to test the proposed interaction torque controller. The X2 robot has four total active degrees of freedom at the hip and knee joints, and passively allows motion at the ankle joints. Each active joint is driven by a Maxon EC60 100 W motor with a 1:122.5 reduction ratio obtained via harmonic gearing and a belt. Copley Accelnet ACK-055-06 motor drivers are used to control the motors. A peak torque of 80 Nm and a peak velocity of 3.2 rad/s can be obtained at each joint.

Due to the high friction caused by the large reduction ratio, it is not feasible to estimate the joint torques by only measuring the current through the motors. Therefore we modified the X2

robot to add joint torque sensors at each driven joint. Each torque sensor consists of a full Wheatstone bridge with four strain gauges on the limb just distal to the joint, similar to the method presented by Claros et al. [29]. These custom joint torque sensors provide measurements with a resolution of 0.3 Nm and 0.1 Nm at the hip and knee joints, respectively. Furthermore, to have a tighter connection with the upper body, an additional trunk brace was adopted from another lower-limb exoskeleton (Exo-H3, Technaid S.L.).

An inertial measurement unit (IMU) (Tech-IMU V4 by Technaid S.L.) is mounted on the backpack to measure the orientation and angular velocity of that link. Using the encoder measurements from each motor and orientation estimation of the backpack, the orientation of each link in the sagittal plane with respect to the gravity vector is estimated. In addition, eight 3-DoF force plates (9047B, Kistler) under a custom instrumented split-belt treadmill are used to measure ground reaction forces at each foot.

Communication with motors and onboard sensors was established over a CAN bus using the CANOpen communication protocol. To minimize communication delay and allow real-time visualization and tuning capabilities, an external PC is connected to the exoskeleton by a tether. Analog force plate readings are acquired with an Arduino Mega board connected to the same PC. The controllers and applications were implemented on a ROS and C++ based open-source software stack called CANOpen Robot Controller (CORC) [30]. High-level controller commands and sensor measurements were updated at 333 Hz, while the low-level current controller of the motors ran at 15 kHz.

B. Dynamic Model

Our proposed WECC control method is based on a whole-body model where we incorporate the sagittal plane dynamics of every link of the exoskeleton, including the backpack.

1) *Whole-body dynamics*: The exoskeleton is modeled as a floating base, a five-link mechanism with four active joints. The dynamics of the human user are not modeled but incorporated into the exoskeleton dynamics as a source of external torque at each joint. For each gait state, the constraints on the system and the equations of motion are modified accordingly. These gait states are no ground contact (*flight*), contact by a single foot (*single stance*), and contact by two feet (*double stance*).

Gait states were estimated using the force plates placed under the split-belt treadmill. Figure 2 presents the state machine structure on gait state estimation.

a) *Flight*: In the flight state, the only external forces on the exoskeleton are due to interaction with the user. The equation of motion in generalized coordinates is

$$\mathbf{M}_{\text{fly}}(\mathbf{q}_{\text{fly}})\ddot{\mathbf{q}}_{\text{fly}} + \mathbf{b}_{\text{fly}}(\mathbf{q}_{\text{fly}}, \dot{\mathbf{q}}_{\text{fly}}) + \mathbf{g}_{\text{fly}}(\mathbf{q}_{\text{fly}}) = S^T \boldsymbol{\tau}_{\text{joint}} + \boldsymbol{\tau}_{\text{int}}, \quad (1)$$

where $\mathbf{q}_{\text{fly}} = [x_0, y_0, \theta_0, \theta_1, \theta_2, \theta_3, \theta_4]$ is a vector of generalized coordinates corresponding to the linear and angular positions of the backpack and the hip and knee joint angles, as shown in Figure 3a. The variable $\mathbf{M}_{\text{fly}} \in \mathbb{R}^{7 \times 7}$ is the mass matrix, $\mathbf{b}_{\text{fly}} \in \mathbb{R}^7$ is a vector of Coriolis and centrifugal forces,



Fig. 1: ExoMotus-X2 lower-limb exoskeleton (left) and its modified version with a user (right).

and $\mathbf{g}_{\text{fly}} \in \mathbb{R}^7$ a vector of gravitational forces. The vector $\boldsymbol{\tau}_{\text{joint}} \in \mathbb{R}^4$ corresponds to joint torques, $S = [0_{4 \times 3}, \mathbb{I}_{4 \times 4}]$ is a selection matrix of actuated joints, and $\boldsymbol{\tau}_{\text{int}} \in \mathbb{R}^7$ is a vector of interaction forces and torques applied to the exoskeleton by the user.

b) *Single stance*: In single stance, the ankle of the stance leg is assumed to be hinged to the ground. With this assumption, the exoskeleton has five degrees of freedom. The generalized coordinates and equations of motion are

$$\mathbf{M}_i(\mathbf{q})\ddot{\mathbf{q}} + \mathbf{b}_i(\mathbf{q}, \dot{\mathbf{q}}) + \mathbf{g}_i(\mathbf{q}) = S^T \boldsymbol{\tau}_{\text{joint}} + \boldsymbol{\tau}_{\text{int}}, \quad i \in \{\text{ls}, \text{rs}\}, \quad (2)$$

where $\mathbf{q} = [\theta_0, \theta_1, \theta_2, \theta_3, \theta_4]$ are the generalized coordinates corresponding to the backpack, hip, and knee angles, as shown in Figure 3b. The matrix and vectors $\mathbf{M}_i \in \mathbb{R}^{5 \times 5}$, $\mathbf{b}_i \in \mathbb{R}^5$, $\mathbf{g}_i \in \mathbb{R}^5$, are the mass matrix, Coriolis and centrifugal torques, and gravitational torques respectively during left stance ($i = \text{ls}$) and right stance ($i = \text{rs}$). The variable $\boldsymbol{\tau}_{\text{joint}} \in \mathbb{R}^4$ corresponds to joint torques, $S = [0_{4 \times 1}, \mathbb{I}_{4 \times 4}]$ is a selection matrix of actuated joints, and $\boldsymbol{\tau}_{\text{int}} \in \mathbb{R}^5$ is a vector of interaction torques applied to the exoskeleton by the user.

c) *Double stance*: This state can be expressed as the single stance state with additional external forces on the swing foot as expressed in Equation (3),

$$\mathbf{M}_i(\mathbf{q})\ddot{\mathbf{q}} + \mathbf{b}_i(\mathbf{q}, \dot{\mathbf{q}}) + \mathbf{g}_i(\mathbf{q}) = S^T \boldsymbol{\tau}_{\text{joint}} + \boldsymbol{\tau}_{\text{int}} + J_j^T \boldsymbol{\Gamma}_j, \quad (3)$$

$$(i, j) \in \{(\text{ls}, \text{r}), (\text{rs}, \text{l})\},$$

where J_j and $\boldsymbol{\Gamma}_j$ corresponds to the contact Jacobian of the left ($j = \text{l}$) or right ($j = \text{r}$) ankle and the external forces at that

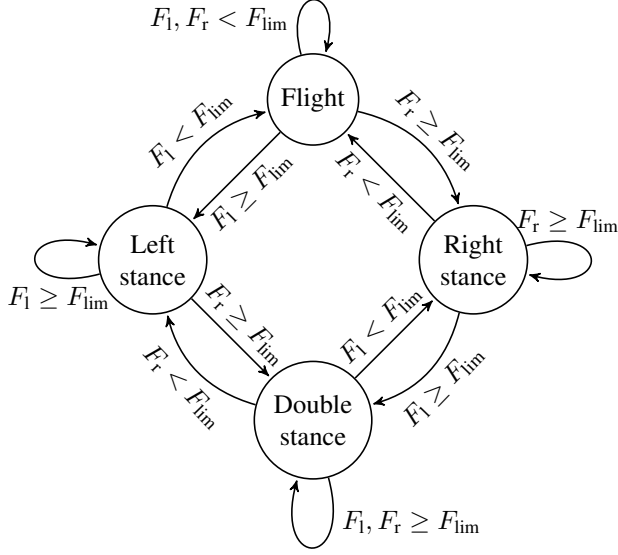


Fig. 2: Gait state machine used in real-time estimation and control. The variables F_l and F_r are left and right vertical force readings, respectively. The threshold force that triggers state change is represented by F_{lim} . States are not allowed to change more than once every 150 ms for robustness to noise.

point, respectively. Multiplying Equation (3) by the transpose of the constraint matrix, $H \in \mathbb{R}^{5 \times 3}$, where $JH = 0$, results in the following equation of motion.

$$H_j^T (M_i(\mathbf{q})\ddot{\mathbf{q}} + \mathbf{b}_i(\mathbf{q}, \dot{\mathbf{q}}) + \mathbf{g}_i(\mathbf{q}) - \boldsymbol{\tau}_{int}) = H_j^T S^T \boldsymbol{\tau}_{joint}, \quad (4)$$

$$(i, j) \in \{(l, r), (r, l)\}.$$

Interested readers may refer to [31] for the details of the constraint matrix H and Equations (3)–(4). It is worth noting that Equation (4) is three-dimensional, which means the system is overactuated during the double stance state. This results in discontinuity in the equation of motion and the dynamic compensation torques during the transitions between single and double stance states. Moreover, the overactuated nature of this state brings additional challenges to the interaction torque estimation, as discussed in Section III.

Due to these challenges, we approximate the double stance state as a transition phase from left stance to right stance or vice versa. The approximated equation of motion at this state is

$$\mathbf{M}_{ds}(\mathbf{q})\ddot{\mathbf{q}} + \mathbf{b}_{ds}(\mathbf{q}, \dot{\mathbf{q}}) + \mathbf{g}_{ds}(\mathbf{q}) = S^T \boldsymbol{\tau}_{joint} + \boldsymbol{\tau}_{int}, \quad (5)$$

where

$$\mathbf{M}_{ds} = \alpha \mathbf{M}_{ls} + (1 - \alpha) \mathbf{M}_{rs}, \quad (6)$$

$$\mathbf{b}_{ds} = \alpha \mathbf{b}_{ls} + (1 - \alpha) \mathbf{b}_{rs}, \quad (7)$$

$$\mathbf{g}_{ds} = \alpha \mathbf{g}_{ls} + (1 - \alpha) \mathbf{g}_{rs}. \quad (8)$$

The variable α in Equations (6)–(8) corresponds to the interpolation factor from left stance dynamics to right stance dynamics and is calculated based on the ratio of the left

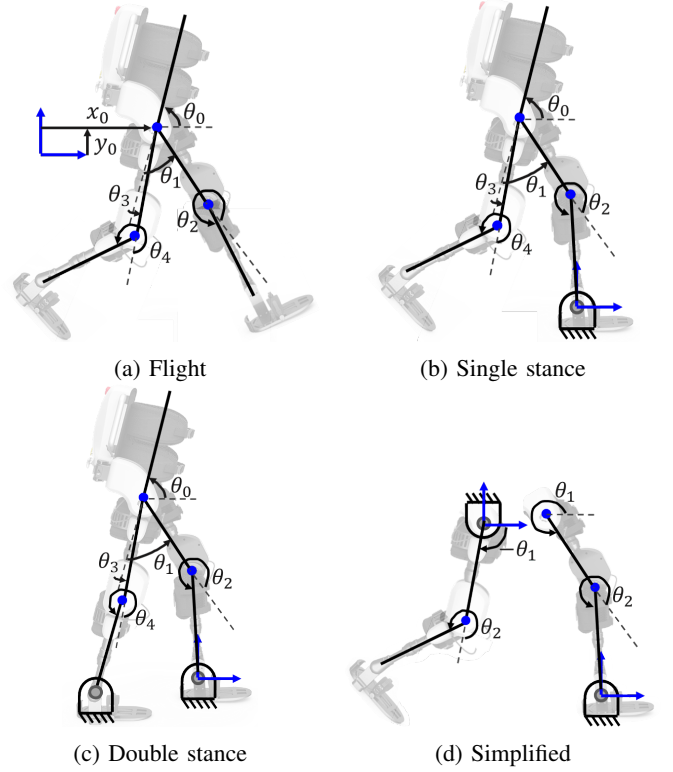


Fig. 3: Different gait states and representation of the generalized coordinates. Whole-body model representations are shown in sub-figures (a), (b), and (c). Sub-figure (d) corresponds to the stance and swing phases of the simplified model.

vertical ground reaction force to the sum of both vertical ground reaction forces,

$$\alpha = \frac{F_{l,y}^{treadmill}}{F_{l,y}^{treadmill} + F_{r,y}^{treadmill}}, \quad (9)$$

where $F_{l,y}^{treadmill}$ and $F_{r,y}^{treadmill}$ are left and right vertical ground reaction forces, respectively. Interpolating the equation of motion from left stance dynamics to right stance dynamics allows smooth continuous modeling of the whole gait cycle during walking. The difference of this method from the work of Camardella et al. [15] is that their kinematic-based gait segmentation is user-dependent and requires a training procedure.

2) *Simplified dynamics*: Modeling each leg of the lower-limb exoskeleton as a double pendulum [14], [19], [23]–[25], [32] is a simpler and commonly used method in the literature. We use this model for comparison to our approach. In this simplified model, each leg is modeled independently from the other and the backpack is not considered. The hip joint is considered grounded for a swing leg, and the ankle joint is considered fixed to the ground for a stance leg, as shown in Figure 3d.

The equation of motion can be written

$$\mathbf{M}_i(\mathbf{q})\ddot{\mathbf{q}} + \mathbf{b}_i(\mathbf{q}, \dot{\mathbf{q}}) + \mathbf{g}_i(\mathbf{q}) = \boldsymbol{\tau}_{joint} + \boldsymbol{\tau}_{int}, \quad i \in \{st, sw\}, \quad (10)$$

where $\mathbf{q} = [\theta_1, \theta_2]$ and $\boldsymbol{\tau}_{joint}$ are the hip and knee joint positions and torques, respectively. The variables $\mathbf{M}_i \in$

TABLE II: Estimated masses and inertias (about axes through the center of mass and perpendicular to the sagittal plane) of links and motor rotors of the X2 exoskeleton.

Link	m [kg]	L [kgm ²]
Backpack	10.3	0.201
Upper thigh	0.7	0.002197
Lower thigh	2.14	0.005901
Upper shank	0.64	0.002346
Lower shank	0.47	0.0007941
Foot	1.25	0.004441
Rotor (apparent)	-	$1.24610^{-4} \times 122.5^2 = 1.87$

TABLE III: Estimated friction parameters of the X2 exoskeleton and R^2 of the fit.

Joint	c_0 [Nm]	c_1 [Nms]	R^2
Left hip	5.01	4.58	0.96
Right hip	3.26	4.67	0.94
Left knee	4.30	3.25	0.96
Right knee	4.45	5.16	0.96

$\mathbb{R}^{2 \times 2}$, $\mathbf{b}_i \in \mathbb{R}^2$, $\mathbf{g}_i \in \mathbb{R}^2$, are the mass matrix, Coriolis and centrifugal torques, and gravitational torques, respectively, during stance ($i = \text{st}$) and swing ($i = \text{sw}$).

C. Parameter Estimation

Inertial parameters such as mass, mass moment of inertia, and center of mass (CoM) locations of each link were estimated from the CAD model of the X2 exoskeleton. Some of these parameters are presented in Table II. Note that the largest inertias come from the apparent inertia of the motor rotors due to the high gear reduction ratios.

The high gear ratios also result in significant friction at each joint. Friction at the joints is modeled as viscous friction combined with Coulomb friction as a function of joint speed,

$$\boldsymbol{\tau}_{\text{friction}} = \mathbf{c}_0 \text{sign } \dot{\boldsymbol{\theta}} + \mathbf{c}_1 \dot{\boldsymbol{\theta}}. \quad (11)$$

To estimate the frictional parameters, the exoskeleton was suspended by backpack attachment points and the motors were driven with sinusoidal torques at varying amplitudes up to 15 Nm and frequencies between 0 and 3 Hz. All joint states were recorded.

As there was no contact with the ground at this configuration, the equation of motion of the flight state was used to estimate the frictional parameters. Equation (1) can be rewritten to include viscous and Coulomb friction constants,

$$\mathbf{M}_{\text{fly}}(\mathbf{q}_{\text{fly}})\ddot{\mathbf{q}}_{\text{fly}} + \mathbf{b}_{\text{fly}}(\mathbf{q}_{\text{fly}}, \dot{\mathbf{q}}_{\text{fly}}) + \mathbf{g}_{\text{fly}}(\mathbf{q}_{\text{fly}}) = S^T(\boldsymbol{\tau}_{\text{motor}} + \mathbf{c}_0 \text{sign } \dot{\boldsymbol{\theta}} + \mathbf{c}_1 \dot{\boldsymbol{\theta}}) + \boldsymbol{\tau}_{\text{int}}. \quad (12)$$

Recorded backpack and joint angular positions, joint angular velocities, joint angular accelerations, and CAD-based inertial parameters were used to calculate the \mathbf{M}_{fly} , \mathbf{b}_{fly} , and \mathbf{g}_{fly} at each time instant. Since the exoskeleton was hung from the backpack at a fixed location, \ddot{x} and \ddot{y} were negligible. Also, as there was no user in the exoskeleton, rotational components of $\boldsymbol{\tau}_{\text{int}}$ were zero. The coefficients \mathbf{c}_0 and \mathbf{c}_1 were solved using least-square minimization based on the recorded motor torques and joint states. Estimated friction parameters for each joint and the R^2 value of the fit are presented in Table III.

III. INTERACTION TORQUE CONTROLLER

A. Interaction Torque Estimation

Estimating the interaction torques between the human and exoskeleton plays a significant role in the transparency and haptic rendering capabilities of the robot. Placing 6 DoF force/torque sensors at every contact point between the human and exoskeleton would theoretically be ideal for measuring the interaction. However, due to the practical challenges of this approach, we chose to estimate the interaction torques through joint torque measurements. Joint torques were measured using our custom joint-torque sensors mentioned in Section II-A.

Because the X2 robot was designed for individuals with sensorimotor impairments and therefore limited walking ability, we estimated the interaction torque during single and double stance only, excluding the flight state.

1) *Single stance interaction torque estimation*: We estimate the interaction torque during single stance by subtracting the gravitational and Coriolis forces from the joint torque readings:

$$\boldsymbol{\tau}_{\text{int}} = -S^T \boldsymbol{\tau}_{\text{joint}} + \mathbf{b}_i(\mathbf{q}, \dot{\mathbf{q}}) + \mathbf{g}_i(\mathbf{q}), \quad i \in \{\text{ls}, \text{rs}\}. \quad (13)$$

The acceleration-dependent inertial component $\mathbf{M}_i \ddot{\mathbf{q}}$ is not subtracted to prevent delays in the estimation as the derivative of the joint velocities needs to be heavily filtered to be used in the estimation.

It is worth noting that $\boldsymbol{\tau}_{\text{int}} \in \mathbb{R}^5$, including the interaction torque on the backpack link in addition to the four leg segments.

2) *Double stance interaction torque estimation*: In the double stance state, with constraints on the ankles hinged to a constant position, the robot has three DoF, while $\boldsymbol{\tau}_{\text{int}} \in \mathbb{R}^5$. Therefore, additional information other than the joint torque measurements is needed to uniquely solve for the interaction torques.

Interaction torque estimation based on left and right stance estimation can be rewritten with the addition of the external ground reaction force at the right and left foot, respectively:

$$\boldsymbol{\tau}_{\text{int}} = -S^T \boldsymbol{\tau}_{\text{joint}} + \mathbf{b}_{\text{ls}}(\mathbf{q}, \dot{\mathbf{q}}) + \mathbf{g}_{\text{ls}}(\mathbf{q}) - J_{\text{r}}^T \mathbf{F}_{\text{r}}^{\text{exo}} \quad (14)$$

$$\boldsymbol{\tau}_{\text{int}} = -S^T \boldsymbol{\tau}_{\text{joint}} + \mathbf{b}_{\text{rs}}(\mathbf{q}, \dot{\mathbf{q}}) + \mathbf{g}_{\text{rs}}(\mathbf{q}) - J_{\text{l}}^T \mathbf{F}_{\text{l}}^{\text{exo}}, \quad (15)$$

where J is the ground contact Jacobian and F^{exo} is the ground reaction force acting on the exoskeleton. Subscripts l and r correspond to left and right, respectively.

Combining Equations 14 and 15 results in ten equations with rank seven. Nine unknowns in these equations are the five-dimensional interaction torque vector and two dimensional ground reaction forces at left ($\mathbf{F}_{\text{l}}^{\text{exo}}$) and right ($\mathbf{F}_{\text{r}}^{\text{exo}}$) foot. Since there are seven independent equations and nine unknowns, it is not possible to uniquely solve for the interaction torque vector without additional information.

To have a unique interaction torque solution, force sensors under the treadmill are used to provide additional information about $\mathbf{F}_{\text{l}}^{\text{exo}}$ and $\mathbf{F}_{\text{r}}^{\text{exo}}$. It is important to distinguish the difference between \mathbf{F}^{exo} and the measured ground reaction forces at the treadmill, $\mathbf{F}^{\text{treadmill}}$. The foot of the exoskeleton has contact with both the ground and user's shoe. Therefore, \mathbf{F}^{exo} equals

to the vector sum of the force applied by the human to the exoskeleton's foot ($\mathbf{F}^{\text{h,foot}}$) and the ground reaction force,

$$\mathbf{F}_i^{\text{exo}} = \mathbf{F}_i^{\text{h,foot}} + \mathbf{F}_i^{\text{treadmill}}, \quad i \in \{l, r\}, \quad (16)$$

where l and r correspond to left and right side, respectively.

The following assumptions are added to solve the interaction torque vector uniquely:

$$\frac{F_{l,y}^{\text{exo}}}{F_{r,y}^{\text{exo}}} = \frac{F_{l,y}^{\text{treadmill}}}{F_{r,y}^{\text{treadmill}}} \quad (17)$$

$$\frac{F_{l,x}^{\text{exo}}}{F_{l,y}^{\text{exo}}} = \frac{F_{l,x}^{\text{treadmill}}}{F_{l,y}^{\text{treadmill}}}, \quad (18)$$

where $F^{\text{treadmill}}$ correspond to the force measured by the split belt treadmill, and subscripts x and y corresponds to the horizontal and vertical component of the force, respectively.

With the addition of Equations 17 and 18 to Equations 14 and 15, interaction torque between the human and the exoskeleton can be uniquely solved during double stance.

3) *Simplified interaction torque estimation*: With the simplified double pendulum model, interaction torques at the hip and knee joints can be estimated by subtracting the dynamical effects from the joint torque measurements:

$$\boldsymbol{\tau}_{\text{int}} = \boldsymbol{\tau}_{\text{joint}} + \mathbf{b}_i(\mathbf{q}, \dot{\mathbf{q}}) + \mathbf{g}_i(\mathbf{q}), \quad i \in \{\text{st, sw}\}. \quad (19)$$

It is important to note that with the simplified method, $\boldsymbol{\tau}_{\text{int}} \in \mathbb{R}^2$ does not include the interaction torque at the backpack. Moreover, because the backpack link is not incorporated into the dynamic model, the backpack's weight is not subtracted, resulting in inaccurate interaction torque estimation for exoskeletons with heavy backpacks.

B. Control

1) *Virtual mass controller*: To control the interaction torques between the human and the exoskeleton, we implemented a *virtual mass controller* [33], [34] to simulate a desired mass or inertia, and no damping, of each generalized coordinate of the exoskeleton. This can be achieved by setting the desired generalized acceleration to

$$\ddot{\mathbf{q}}^* = \mathbf{M}_{\text{virt}}^{-1}(\boldsymbol{\tau}_{\text{int}} - \boldsymbol{\tau}_{\text{int}}^*), \quad (20)$$

where $\boldsymbol{\tau}_{\text{int}}^*$ is the desired interaction torque, e.g., zero for transparency or nonzero for other desired impedances.

Under the assumptions of perfect control of the generalized accelerations and accurate interaction torque estimation with little delay, this equation shows that the interaction torque error is proportional to the chosen virtual mass matrix \mathbf{M}_{virt} and joint accelerations. Therefore, lowering \mathbf{M}_{virt} results in better interaction torque tracking. Obviously, \mathbf{M}_{virt} cannot be decreased below a certain limit due to the actuation limits, modeling errors, and communication delays. We used a diagonal \mathbf{M}_{virt} and tuned the virtual mass parameter for each generalized coordinate independently, reducing each virtual mass as much as possible before compromising the stability of the control. This process resulted in different virtual mass parameters for single stance and double stance, as shown in Table IV. The virtual inertia of the backpack is relatively large to allow better control performance at the leg segments.

TABLE IV: Virtual mass values for each link.

Link	Gait State	Virtual Mass [kgm ²]
Backpack	Single Stance	2
Backpack	Double Stance	3.5
Thigh	Single Stance	0.7
Thigh	Double Stance	1.2
Shank	Single Stance	0.5
Shank	Double Stance	0.87

2) *Constrained optimization*: While the desired acceleration $\ddot{\mathbf{q}}^*$ in Equation (20) is a five-dimensional vector, the robot has only four actuated joints. Therefore, it is not possible to perfectly track the desired generalized accelerations calculated by the virtual mass controller. Moreover, the maximum torque, power, and velocity of the motors bring additional limitations. To track the desired generalized acceleration as accurately as possible under physical and safety constraints, we use real-time constrained optimization with OSQP [35] to solve for $\mathbf{x} = (\ddot{\mathbf{q}}, \boldsymbol{\tau}_{\text{motor}}) \in \mathbb{R}^9$, where $\boldsymbol{\tau}_{\text{motor}}$ is a vector of torques sent to the drivers:

$$\begin{aligned} \min_{\mathbf{x}} \quad & \|f(\mathbf{x})\| \\ \text{s.t.} \quad & \mathbf{A}\mathbf{x} = \mathbf{b} \\ & \mathbf{D}\mathbf{x} \leq \mathbf{f}. \end{aligned} \quad (21)$$

The objective function $\|f(\mathbf{x})\|$ is the 2-norm of the difference between the actual and desired generalized accelerations,

$$f(\mathbf{x}) = [\mathbb{I}_{5 \times 5}, \mathbf{0}_{5 \times 4}]\mathbf{x} - \ddot{\mathbf{q}}^*. \quad (22)$$

The equality constraint ensures that optimized variables satisfy the equation of motion of the corresponding gait state under physical limits.

$$\mathbf{A} = \mathbf{A}_{\text{EOM}} = [\mathbf{M}_i, -\mathbf{S}^\top],$$

$$\mathbf{b} = \mathbf{b}_{\text{EOM}} = [-\mathbf{b}_i - \mathbf{g}_i + \boldsymbol{\tau}_{\text{int}} + \mathbf{S}^\top(\mathbf{c}_0 \text{sign } \dot{\boldsymbol{\theta}} + \mathbf{c}_1 \dot{\boldsymbol{\theta}})], \quad (23)$$

where $i \in \{\text{ls, rs, ds}\}$.

Inequality constraints arise from physical and safety constraints on motor torque, power, and velocity. Motor torque and power constraints are presented in Equations (24) and (25), respectively:

$$\mathbf{D}_{\boldsymbol{\tau}_{\text{max}}^+} = [0_{4 \times 5}, \mathbb{I}_{4 \times 4}], \quad \mathbf{f}_{\boldsymbol{\tau}_{\text{max}}^+} = \boldsymbol{\tau}_{\text{max}} \quad (24)$$

$$\mathbf{D}_{\boldsymbol{\tau}_{\text{max}}^-} = [0_{4 \times 5}, -\mathbb{I}_{4 \times 4}], \quad \mathbf{f}_{\boldsymbol{\tau}_{\text{max}}^-} = \boldsymbol{\tau}_{\text{max}},$$

$$\mathbf{D}_{\mathcal{P}_{\text{max}}^+} = [0_{4 \times 5}, \mathbb{I}_{4 \times 4}], \quad \mathbf{f}_{\mathcal{P}_{\text{max}}^+} = \frac{\mathcal{P}_{\text{max}}}{|\dot{\mathbf{q}}|} \quad (25)$$

$$\mathbf{D}_{\mathcal{P}_{\text{max}}^-} = [0_{4 \times 5}, -\mathbb{I}_{4 \times 4}], \quad \mathbf{f}_{\mathcal{P}_{\text{max}}^-} = \frac{\mathcal{P}_{\text{max}}}{|\dot{\mathbf{q}}|},$$

where $\boldsymbol{\tau}_{\text{max}} = 80$ Nm and $\mathcal{P}_{\text{max}} = 100$ W are the maximum allowable torque and power of the motors, respectively.

The joint velocity constraint is converted to an acceleration constraint such that the velocity at the next time step will not exceed maximum velocity limits,

$$\begin{aligned} \mathbf{D}_{\dot{\mathbf{q}}^+} &= [0_{4 \times 1}, \mathbb{I}_{4 \times 4}, 0_{4 \times 4}], \quad \mathbf{f}_{\dot{\mathbf{q}}^+} = \frac{\dot{\mathbf{q}}_{\text{max}} - \dot{\mathbf{q}}}{\Delta t} \\ \mathbf{D}_{\dot{\mathbf{q}}^-} &= [0_{4 \times 1}, -\mathbb{I}_{4 \times 4}, 0_{4 \times 4}], \quad \mathbf{f}_{\dot{\mathbf{q}}^-} = \frac{\dot{\mathbf{q}}_{\text{max}} + \dot{\mathbf{q}}}{\Delta t}, \end{aligned} \quad (26)$$

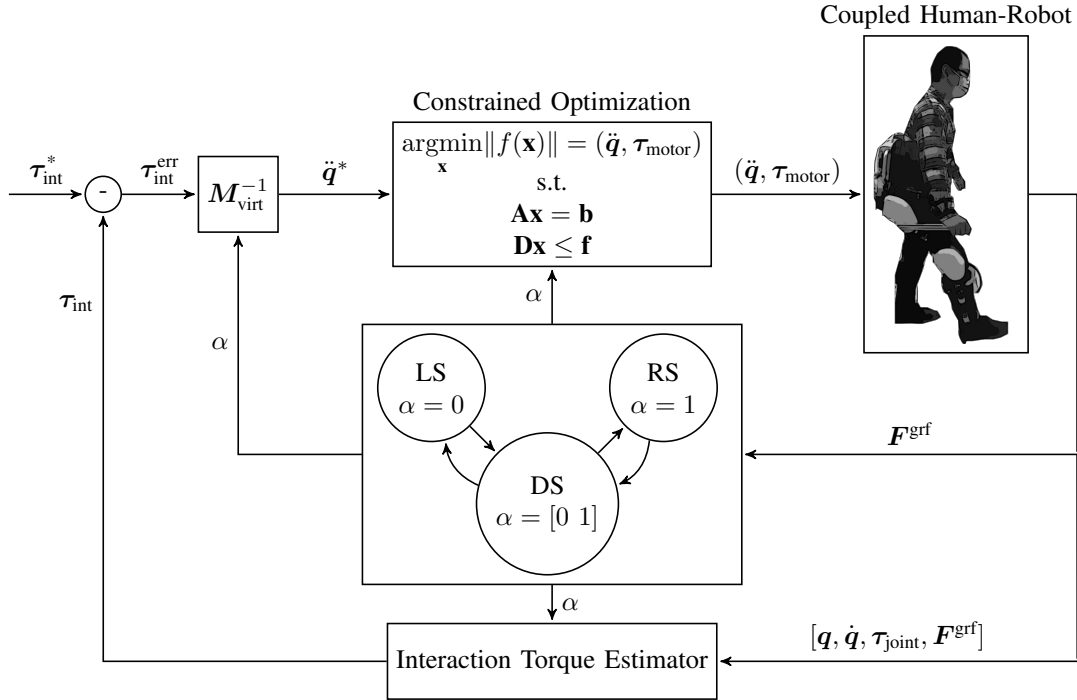


Fig. 4: Schematic of the interaction force controller.

where $\dot{q}_{max} = 3.0$ rad/s and $\Delta t = 0.003$ s is the control loop period. Individual \mathbf{D} matrices and \mathbf{f} vectors in Equations (24)–(26) are vertically stacked to obtain the overall \mathbf{D} matrix and \mathbf{f} vector in Equation (21). The controller is illustrated in Figure 4.

Because we have only a single objective function for this task, a constrained optimization suffices. In the case of multiple objectives with different priorities, a hierarchical optimization framework could be applied [36], [37]. This allows optimization of lower-priority tasks using freedoms in the design vector that do not affect the objective functions of higher-priority tasks.

IV. EXPERIMENTAL VALIDATION

Three healthy subjects (one male, two female, 71.6 ± 12.9 kg, 174 ± 1.7 cm, 29 ± 2.6 years) participated in this study to test the proposed interaction torque controller. The link lengths of the exoskeletons were adjusted for each participant so that they were comfortable and their joints were aligned with the exoskeleton's. None of the subjects had used a lower-limb exoskeleton before this study. At the beginning of the experiment, subjects were allowed about two minutes of walking with the exoskeleton on a treadmill for familiarization. We tested the haptic rendering capabilities for zero desired interaction torque under three conditions and nonzero desired interaction torques under two different conditions. In addition to the proposed controller (WECC), the following two conditions were tested:

a) No-drive: A passive exoskeleton with disassembled drives was used. This allowed us to eliminate the main sources of friction and inertia, which are the apparent rotor inertias. Subjects still felt the weight of the exoskeleton, however.

b) Simplified: Legs are modeled and controlled as independent double pendulums. Interaction torques are calculated with the simplified model as in Equation (19). Furthermore, Equation (10) is used as the forward model to track the desired acceleration commands sent by the virtual mass controller (Equation (20)). The simplified interaction torque estimation is used in the control loop; however, the presented interaction torque results are calculated using the whole-body model to compare the results between conditions.

The institutional review board (IRB) of Northwestern University approved this study (STU00212684), and all procedures were in accordance with the Declaration of Helsinki.

A. Evaluation of Transparency

Haptic transparency was tested for our proposed WECC method, double-pendulum based simplified controller, and passive no-drive condition. For the WECC and simplified controllers with actuation, zero desired interaction torque was commanded for each generalized coordinate. Each condition was tested for three trials of one-minute walking on a treadmill with a speed of 1.1 km/h. A relatively slow speed was selected due to usual walking training speeds in physical rehabilitation settings and the joint velocity limitation of 3.2 rad/s of the ExoMotus-X2 exoskeleton. Trials of the WECC and simplified controllers were performed in a randomized order for each subject. All trials of the passive no-drive condition were performed consecutively for practical reasons, as this condition requires a different exoskeleton with disassembled drives. A metronome was played at 40 bpm, and subjects were asked to synchronize their heel strikes with the beats of the metronome to have similar step lengths between subjects and trials.

TABLE V: Virtual stiffness and damping values used for haptic rendering evaluation.

Joint	Leg Phase	k_i [Nm/rad]	c_i [Nms/rad]	q_i^* [degrees]
Hip	Stance	50	10	25
Hip	Swing	30	6	25
Knee	Stance	30	6	-45
Knee	Swing	25	5	-45

Human-exoskeleton interaction torques and muscle activity were used to assess the transparency performance.

B. Evaluation of Haptic Rendering

We tested the interaction torque rendering capabilities of the proposed WECC controller and the simplified controller when the desired interaction torques are generated by virtual springs and dampers at the joints,

$$\tau_{\text{int}}^* = \mathbf{K}(\mathbf{q} - \mathbf{q}^*) + \mathbf{C}\dot{\mathbf{q}}, \quad (27)$$

where \mathbf{q}^* is the neutral position vector of the virtual springs and \mathbf{K} and \mathbf{C} are diagonal stiffness and damping matrices, respectively. A constant q_i^* was used at each joint i , and the desired interaction torque at backpack was set to zero. Since the motion of a leg during stance is slower and has a smaller range, larger stiffness and damping constants were used for a leg's stance phase than for its swing phase. The diagonal values of the stiffness (k_i) and damping (c_i) matrices, as well as \mathbf{q}^* , are presented in Table V. To avoid discontinuities in the desired interaction torque during stance to swing transitions, the desired interaction torque was low-pass filtered with a cutoff frequency of 5 Hz.

C. Data Recording and Analysis

Joint positions, velocities, and interaction torques were recorded during all trials. The exoskeleton without drives is instrumented with IMUs (Tech-IMU V4, Technaid, Spain) at each link to measure joint kinematics, which is used in interaction torque calculation. All exoskeleton data were collected at 333 Hz.

Nine bipolar electromyography (EMG) electrodes (MA400 EMG Systems, Motion Lab Systems, USA) were placed on the belly of the following muscles for the evaluation of transparency experiments: rectus femoris (RF), vastus lateralis (VL), vastus medialis (VM), biceps femoris (BF), semitendinosus (ST), medial gastrocnemius (MG), lateral gastrocnemius (LG), and soleus (SOL). The electrodes were placed only on the left leg. EMG data were recorded at 1500 Hz. The raw EMG signals were first bandpass filtered between 20 and 500 Hz with a sixth-order Butterworth filter. Then, a notch filter between 59 and 61 Hz was applied to reduce noise due to power line interference. Finally, the signals were low-pass filtered at 10 Hz after full-wave rectification. Processed EMG signals were normalized with respect to the mean of the no-drive condition for each subject independently. For one subject, RF recordings were not successfully collected due to sensor failure.

Exoskeleton-based measurements and processed EMG readings were windowed between the heel strikes of the corresponding leg. Windowed data from the same joint on both legs and three subjects were lumped together for each condition. The mean absolute value of the whole cycle and only stance or swing phases for each gait cycle were used as sample points and visualized in the corresponding box plots in the Results section. Three-way ANOVA analysis with the condition, subjects, and trial number of a subject as random variables was applied to test statistical significance between the means of each condition for each measure (i.e., interaction torque, muscle activity). A p-value of $p = 0.05$ was used to accept or reject null hypotheses.

V. RESULTS

A. Transparency

Interaction torques during the transparency trials, normalized by the body mass of each subject (units of Nm/kg), are presented in Figure 5 and Table VI. Below we describe the interaction torques during a leg's swing phase, its stance phase (both single stance and double stance unless otherwise noted), and its entire cycle.

For both hip and knee joints, interaction torques with the proposed WECC controller were mostly bounded to the range ± 0.13 Nm/kg, with little difference between stance and swing phases. In contrast, the simplified controller resulted in hip and knee peak torques of 0.5 Nm/kg and 0.4 Nm/kg, respectively, at the end of the single stance state. Similarly, the no-drive condition resulted in peak torques of 0.4 Nm/kg and 0.5 Nm/kg at the hip and knee joints, respectively.

The performance of the proposed WECC controller was consistent throughout the whole gait cycle with a mean absolute interaction torque around 0.07 ± 0.02 Nm/kg both at the hip and knee joints during both stance and swing phases. The simplified controller resulted in a similar mean absolute interaction torque during the swing phase ($\Delta \leq 0.01$ Nm/kg) but significantly higher mean absolute interaction torque at the hip and knee joints, respectively, during the stance phase ($\Delta \geq 0.13$ Nm/kg, $p < 0.01$). During the stance phase, higher interaction torques were observed for the no-drive condition than for WECC at both the hip ($\Delta \geq 0.12$ Nm, $p < 0.01$) and knee ($\Delta \geq 0.24$ Nm/kg, $p < 0.01$) joints. During the swing phase, the no-drive condition resulted in significantly higher interaction torques at the hip joint ($\Delta \geq 0.10$ Nm/kg, $p < 0.01$) and similar interaction torques at the knee joint ($\Delta \approx 0.01$ Nm/kg) compared to the proposed WECC method. Average transparency performance during the whole cycle was best for the WECC controller, with mean absolute interaction torques of 0.076 ± 0.020 Nm/kg and 0.071 ± 0.021 Nm/kg at the hip and knee joints, respectively. The simplified controller achieved better mean absolute interaction torque than the no-drive condition at the knee joint ($\Delta \approx 0.07$ Nm/kg) averaged over the whole gait cycle. At the hip joint, both performances were similar with a mean interaction torque difference around 0.01 Nm/kg.

Figure 6 and Table VII show the muscle activity of the various muscles during the transparency trials. It is seen that

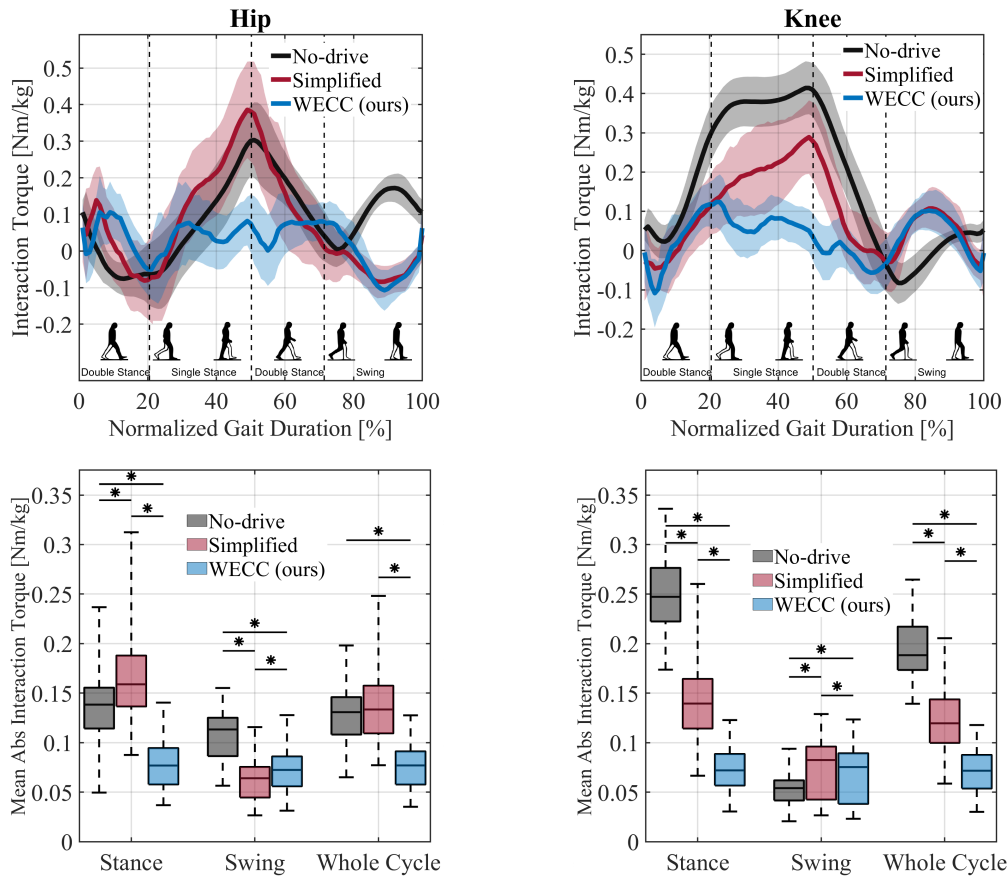


Fig. 5: Interaction torques between the human and robot during transparency trials. The figures on the top row show the interaction torques vs. normalized gait duration. The data includes every step of both legs of all three subjects and the shaded area represents one standard deviation. On the bottom row, the box and whisker plots of the mean absolute interaction torques during the stance phase, swing phase, and the whole gait cycle are presented. Mean absolute values of the corresponding phase at each step of both legs of all three subjects are used as a data point in box and whisker plots ($N \approx 320$).

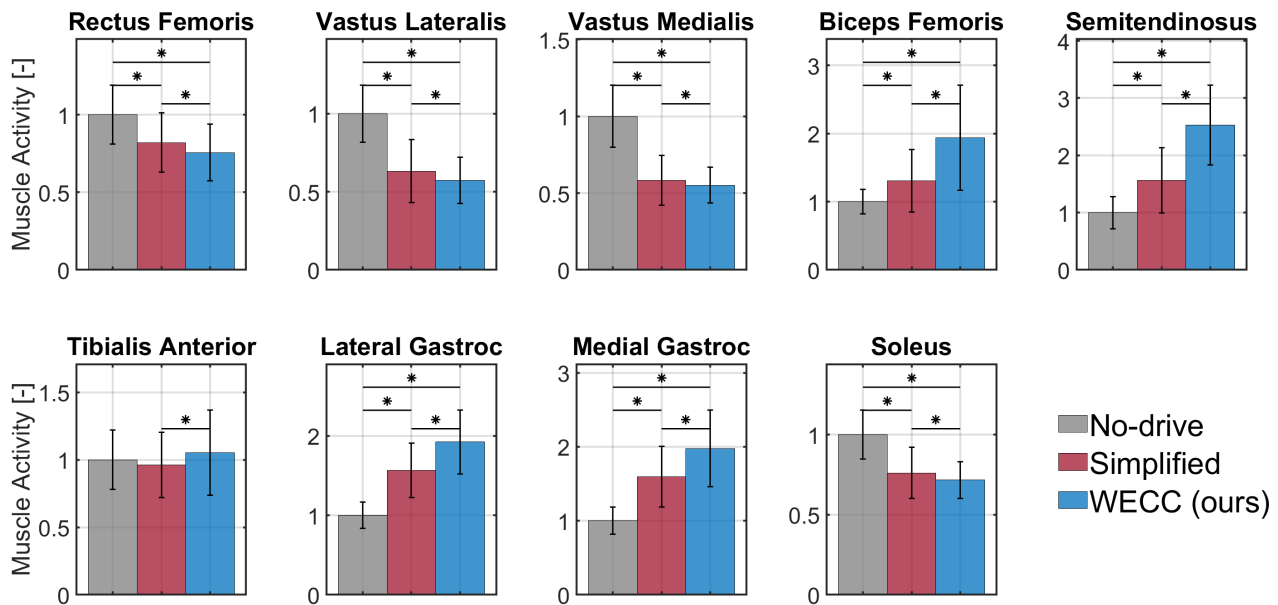


Fig. 6: Muscle activity during transparency experiments. Data are normalized with respect to the mean of the no-drive condition. Mean absolute values of the filtered EMG data averaged over the whole cycle at each step of all subjects are used as a data point in bar plots ($N \approx 160$).

TABLE VI: Mean and standard deviation of the interaction torques between the human and robot at hip and knee joints during transparency experiments. All values are expressed in Nm/kg.

Joint	Leg Phase	No-drive	Simplified	WECC (ours)
Hip	Stance	0.13 ± 0.033	0.16 ± 0.036	0.077 ± 0.021
Hip	Swing	0.11 ± 0.023	0.062 ± 0.019	0.072 ± 0.020
Hip	Whole cycle	0.13 ± 0.025	0.14 ± 0.031	0.076 ± 0.020
Knee	Stance	0.25 ± 0.034	0.14 ± 0.033	0.072 ± 0.020
Knee	Swing	0.052 ± 0.015	0.074 ± 0.028	0.068 ± 0.026
Knee	Whole cycle	0.19 ± 0.028	0.12 ± 0.029	0.071 ± 0.021

TABLE VII: Mean and standard deviation of muscle activities during transparency experiments, normalized with respect to the mean of the no-drive condition.

Muscle	Simplified	WECC (ours)
RF	0.83 ± 0.18	0.77 ± 0.18
VL	0.64 ± 0.21	0.59 ± 0.15
VM	0.59 ± 0.16	0.56 ± 0.10
BF	1.32 ± 0.46	1.94 ± 0.76
ST	1.57 ± 0.58	2.51 ± 0.7
TA	0.97 ± 0.24	1.06 ± 0.31
LG	1.56 ± 0.35	1.91 ± 0.39
MG	1.58 ± 0.39	1.95 ± 0.49
SOL	0.76 ± 0.19	0.72 ± 0.12

muscles responsible for hip flexion (RF) and knee extension (RF, VL, VM) had the lowest activation with our WECC controller and highest with the passive no-drive condition. On the other hand, our controller resulted in the most activity, and no-drive condition resulted in the least activity, for the muscles responsible for hip extension and knee flexion (BF, ST). Furthermore, the SOL muscle, responsible for ankle plantarflexion, was used the least with our WECC controller and the most under the no-drive condition. In contrast, LG and MG muscles, responsible for knee flexion and ankle plantarflexion, had the highest activation with our WECC controller and the lowest under the no-drive condition.

B. Haptic Rendering

Properties of the rendered virtual spring-damper elements shown in Table V resulted in the desired interaction torques presented in Figure 7. The figure includes data from the joints of both legs and three subjects. Desired interaction torques vary in the range ± 15 Nm during the gait cycle for all subjects.

TABLE VIII: Mean and standard deviation of the interaction torque error between the human and robot at hip and knee joints during haptic rendering experiments. All values are expressed in Nm/kg.

Joint	Leg Phase	Simplified	WECC (ours)
Hip	Stance	0.120 ± 0.032	0.048 ± 0.014
Hip	Swing	0.038 ± 0.092	0.039 ± 0.010
Hip	Whole cycle	0.096 ± 0.026	0.046 ± 0.012
Knee	Stance	0.210 ± 0.039	0.051 ± 0.014
Knee	Swing	0.041 ± 0.013	0.049 ± 0.014
Knee	Whole cycle	0.170 ± 0.032	0.050 ± 0.013

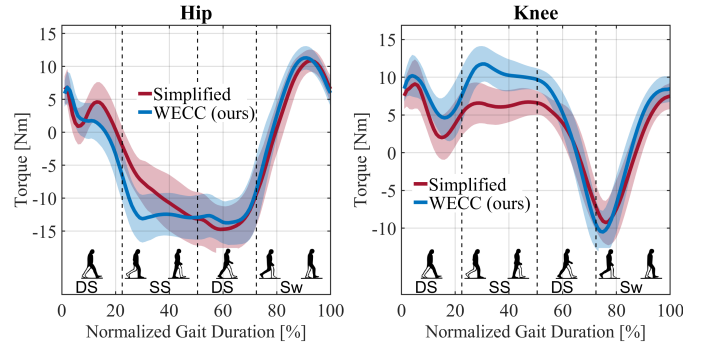


Fig. 7: Desired interaction torque due to the rendered spring damper elements.

The rendering performance of our proposed WECC controller and the simplified controller are shown in Figure 8 and Table VIII. Similar to the performance of transparency trials, our controller’s interaction torque tracking error was mostly bounded between ± 0.1 Nm/kg during the whole gait cycle. On the other hand, the simplified controller resulted in peak normalized interaction torque errors of 0.3 Nm/kg and 0.45 Nm/kg at the hip and knee joints, respectively, near the end of the single stance state.

Our WECC controller resulted in normalized mean absolute interaction torque error of 0.049 ± 0.014 Nm/kg and 0.039 ± 0.010 Nm/kg at the hip joint during the stance and swing phases, respectively. The simplified controller resulted in a similar mean absolute error during the swing phase both at the hip and knee joints ($\Delta < 0.01$ Nm/kg). On the other hand, the average absolute interaction torque error was significantly larger during the stance phase both at the hip ($\Delta > 0.1$ Nm/kg, $p < 0.05$) and knee ($\Delta > 0.2$ Nm/kg, $p < 0.05$) joints. Averaged over the whole cycle, our WECC controller resulted in an error of 0.050 ± 0.012 Nm/kg for both hip and knee joints. The errors of the simplified controller were significantly larger both at the hip ($\Delta > 0.05$ Nm/kg, $p < 0.05$) and knee joints ($\Delta > 0.1$ Nm/kg, $p < 0.05$).

VI. DISCUSSION

A. Interaction Torque Tracking

The simplified controller and the proposed WECC controller performed similarly during the swing phase for both joints in the transparency and haptic rendering trials, as shown in Figures 5 and 8. Since the swing leg is not affected by the weight of the backpack and the other leg, the two-link simplified model is sufficient and results in accurate interaction torque estimation and motor torque calculation for the swing leg. On the other hand, the simplified controller failed to render the desired interaction torques for the stance leg. This is because the model does not consider whole-body dynamics, resulting in incorrect interaction torque estimation for the stance leg. For the simplified controller, subjects feel additional torques on their joints due to the uncompensated weight of the robot. As the proposed WECC controller uses whole-body dynamics and considers physical limitations, the interaction torque tracking performance was consistent throughout the entire gait cycle.

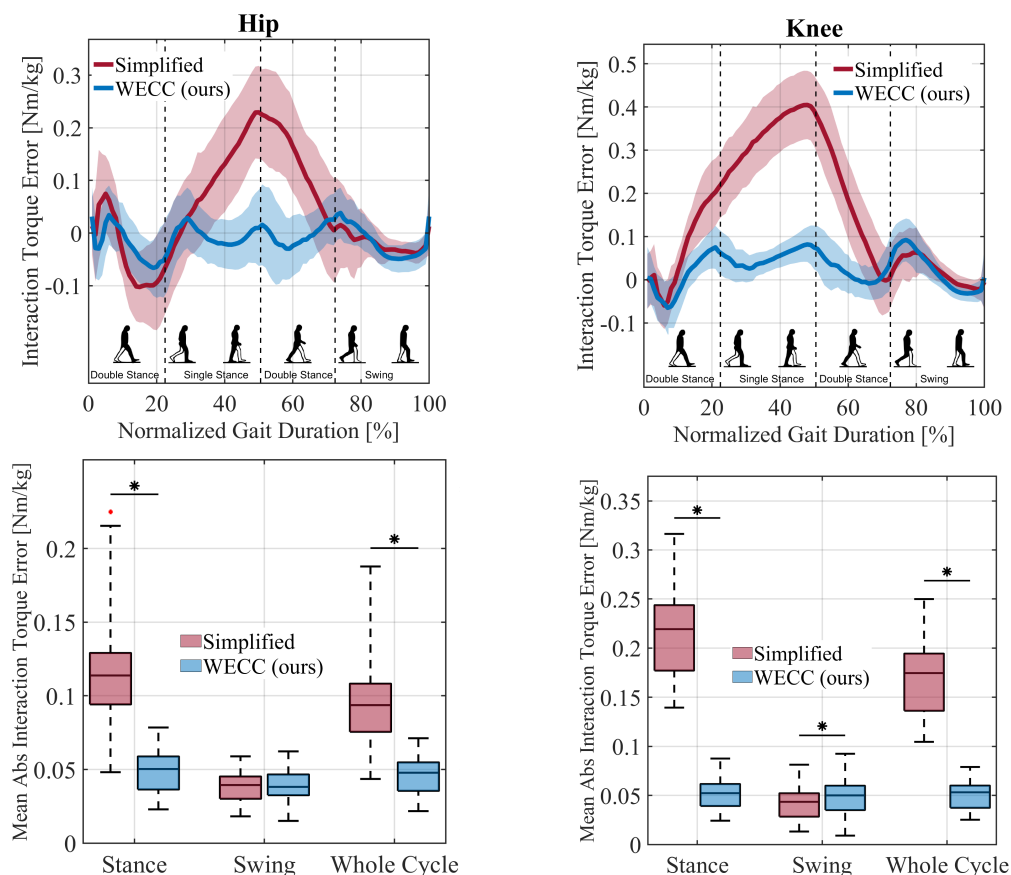


Fig. 8: Interaction torque error during haptic rendering trials. The figures on the top row show the interaction torque error vs. normalized gait duration. The data includes every step of both legs of all three subjects and the shaded area represents one standard deviation. On the bottom row, the box and whisker plots of the mean absolute interaction torque error during the stance phase, swing phase, and the whole gait cycle are presented. Mean absolute values of the corresponding phase at each step of both legs of all three subjects are used as a data point in box and whisker plots ($N \approx 370$).

The most transparent performance at the knee joint was obtained during the swing phase of the no-drive condition. This is because the weight of the shank is insignificant, and there is low friction and no apparent rotor inertia. As the weight of the whole leg becomes more significant, the no-drive condition results in more interaction torque at the hip joint compared to active controllers, where the weight of the leg is compensated. The highest amount of torque was observed for the stance leg under the no-drive condition as the stance leg of the subject needs to overcome the torques appearing due to the weight of the robot’s stance leg, swing leg, and backpack.

B. Muscle Activity

The muscles responsible for hip flexion (RF) and knee extension (RF, VL, VM) were activated the least with the proposed WECC controller and the most with the passive no-drive condition during the transparency trials. This is mainly due to the accurate compensation of the exoskeleton dynamics for the WECC controller.

The opposite trend was observed for the muscles responsible for hip extension and knee flexion (BF, ST). These muscles were activated more with the WECC controller and less with

the no-drive condition. Figure 9 shows the interaction power for all conditions with respect to the normalized gait duration. The simplified controller and no-drive exoskeleton actually assist the hip extension motion during the single stance state. At first glance, it might be surprising that the passive exoskeleton provides assistance in some instances; however, this is due to the weight of the exoskeleton, which results in torques driving hip extension and knee flexion. These results are also in line with the findings of MacLean et al. [38], who observed higher BF activity with increasing weight support while walking at a similar speed as in our setup.

The gastrocnemius muscles (LG, MG), which are responsible for ankle plantarflexion and knee flexion, were activated most with the WECC controller and least with the no-drive condition. On the other hand, an opposite trend was observed for the SOL muscle, which is responsible for ankle plantarflexion. High interaction torques towards the knee-flexion direction (positive direction in Figure 5) for the simplified and no-drive conditions leads to less gastrocnemius activity in these conditions. This explains the different trend between gastrocnemius and SOL muscles.

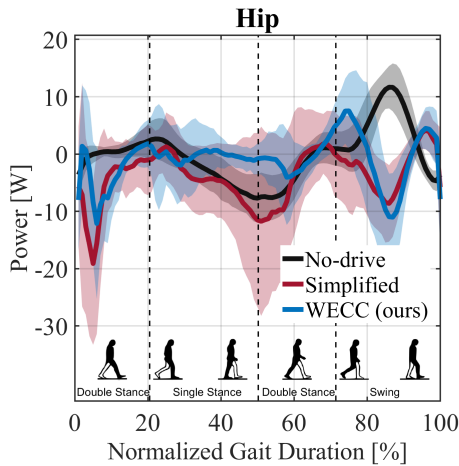


Fig. 9: Hip interaction power during transparency experiments. Positive and negative values indicate resistance and assistance to the human, respectively.

VII. CONCLUSION

We have presented the whole-exoskeleton closed-loop compensation (WECC) controller to measure and control the interaction torques between a user and a floating base hip-knee exoskeleton that contacts the ground. WECC controller calculates the interaction torques using joint torque measurements and gait state information. The desired joint interaction torques are achieved by using a virtual mass controller together with a constrained optimization scheme that considers the whole-exoskeleton dynamics, physical limits, and safety constraints. The performance of WECC controller was compared in terms of transparency and spring-damper haptic rendering with a commonly used simplified double-pendulum model where the legs are modeled independent of one another. WECC control resulted in consistent interaction torque tracking during the whole gait cycle for both zero and nonzero desired interaction torques, while the simplified controller failed to track desired interaction torques during the stance phase.

Future improvements to WECC control could include explicit modeling of joint limits in the dynamic model especially since the knee joint gets close to the physical limit during the gait cycle. This will improve the accuracy of the forward model and therefore the tracking of the optimized accelerations. Moreover, an inner acceleration loop to compensate for the modeling inaccuracies, using additional IMUs or reinforcement-based strategies [39] for online optimization of system parameters, may be an option to improve the current results. Additional IMUs or pressure insoles can also be used to substitute the sensorized treadmill to estimate the continuous gait state.

WECC controller can be used to adjust the interaction torques to assist a user in overground walking, to resist for training in a clinical setting, or to provide haptic transparency. WECC control is especially beneficial for heavy lower-limb exoskeletons where the whole-body dynamics need to be compensated. In future studies, this infrastructure will be used to investigate the effects of dyadic haptic interaction on

performance and learning for complex multi-DOF lower-limb motions [40]–[42].

ACKNOWLEDGMENT

We would like to thank Tim Haswell for his technical support on the hardware improvements of the ExoMotus-X2 exoskeleton.

REFERENCES

- [1] J. C. Moreno, J. Figueiredo, and J. L. Pons, *Chapter 7 - Exoskeletons for lower-limb rehabilitation*. Elsevier Ltd., 2018.
- [2] W. Huo, S. Mohammed, J. C. Moreno, and Y. Amirat, "Lower limb wearable robots for assistance and rehabilitation: A state of the art," *IEEE Systems Journal*, vol. 10, no. 3, pp. 1068–1081, 2016.
- [3] G. S. Sawicki, O. N. Beck, I. Kang, and A. J. Young, "The exoskeleton expansion: Improving walking and running economy," *Journal of NeuroEngineering and Rehabilitation*, vol. 17, no. 1, pp. 1–9, 2020.
- [4] L. Marchal-Crespo, P. Tsangaris, D. Obwegeser, S. Maggioni, and R. Riener, "Haptic error modulation outperforms visual error amplification when learning a modified gait pattern," *Front Neurosci*, vol. 13, p. 61, Feb. 2019.
- [5] H.-J. Lee, S. Lee, W. H. Chang, K. Seo, Y. Shim, B.-O. Choi, G.-H. Ryu, and Y.-H. Kim, "A wearable hip assist robot can improve gait function and cardiopulmonary metabolic efficiency in elderly adults," *IEEE Transactions on Neural Systems and Rehabilitation Engineering*, vol. 25, no. 9, pp. 1549–1557, 2017.
- [6] B. Hobbs and P. Artemiadis, "A Review of Robot-Assisted Lower-Limb Stroke Therapy: Unexplored Paths and Future Directions in Gait Rehabilitation," *Frontiers in Neurobotics*, vol. 14, no. April, 2020.
- [7] R. Baud, A. R. Manzoori, A. Ijspeert, and M. Bouri, "Review of control strategies for lower-limb exoskeletons to assist gait," *Journal of NeuroEngineering and Rehabilitation*, vol. 18, no. 1, p. 119, Jul 2021.
- [8] L. Marchal-Crespo and D. J. Reinkensmeyer, "Review of control strategies for robotic movement training after neurologic injury," *Journal of NeuroEngineering and Rehabilitation*, vol. 6, no. 1, p. 20, Jun 2009.
- [9] G. Colombo, M. Joerg, R. Schreier, V. Dietz, *et al.*, "Treadmill training of paraplegic patients using a robotic orthosis," *Journal of rehabilitation research and development*, vol. 37, no. 6, pp. 693–700, 2000.
- [10] S. K. Banala, S. K. Agrawal, and J. P. Scholz, "Active Leg Exoskeleton (ALEX) for gait rehabilitation of motor-impaired patients," *2007 IEEE 10th International Conference on Rehabilitation Robotics, ICORR'07*, vol. 00, no. c, pp. 401–407, 2007.
- [11] J. F. Veneman, R. Kruidhof, E. E. G. Hekman, R. Ekkelenkamp, E. H. F. Van Asseldonk, and H. van der Kooij, "Design and evaluation of the Lopes exoskeleton robot for interactive gait rehabilitation," *IEEE Transactions on Neural Systems and Rehabilitation Engineering*, vol. 15, no. 3, pp. 379–386, 2007.
- [12] S. A. Murray, K. H. Ha, C. Hartigan, and M. Goldfarb, "An assistive control approach for a lower-limb exoskeleton to facilitate recovery of walking following stroke," *IEEE Transactions on Neural Systems and Rehabilitation Engineering*, vol. 23, no. 3, pp. 441–449, 2015.
- [13] A. Tsukahara, K. Yoshida, A. Matsushima, K. Ajima, C. Kuroda, N. Mizukami, and M. Hashimoto, "Effects of gait support in patients with spinocerebellar degeneration by a wearable robot based on synchronization control," *Journal of NeuroEngineering and Rehabilitation*, vol. 15, no. 1, p. 84, Sep 2018.
- [14] L. J. Mayag, M. Múnera, and C. A. Cifuentes, "Human-in-the-Loop Control for AGORA Unilateral Lower-Limb Exoskeleton," *Journal of Intelligent and Robotic Systems: Theory and Applications*, vol. 104, no. 1, 2022.
- [15] C. Camardella, F. Porcini, A. Filippeschi, S. Marcheschi, M. Solazzi, and A. Frisoli, "Gait Phases Blended Control for Enhancing Transparency on Lower-Limb Exoskeletons," *IEEE Robotics and Automation Letters*, vol. 6, no. 3, pp. 5453–5460, 2021.
- [16] J. Vanilt, K. Tanghe, M. Afschrift, A. K. Bruijnes, K. Junius, J. Geeroms, E. Aertbeliën, F. De Groot, D. Lefeber, I. Jonkers, and J. De Schutter, "Model-based control for exoskeletons with series elastic actuators evaluated on sit-to-stand movements," *Journal of NeuroEngineering and Rehabilitation*, vol. 16, no. 1, p. 65, Jun 2019.
- [17] R. M. Andrade, S. Sapienza, and P. Bonato, "Development of a 'transparent operation mode' for a lower-limb exoskeleton designed for children with cerebral palsy," *IEEE International Conference on Rehabilitation Robotics*, vol. 2019-June, pp. 512–517, 2019.

- [18] R. M. Andrade, S. Sapienza, E. E. Fabara, and P. Bonato, "Trajectory tracking impedance controller in 6-dof lower-limb exoskeleton for overground walking training: Preliminary results," in *2021 International Symposium on Medical Robotics (ISMR)*, 2021, pp. 1–6.
- [19] Y. Tu, A. Zhu, J. Song, H. Shen, Z. Shen, X. Zhang, and G. Cao, "An adaptive sliding mode variable admittance control method for lower limb rehabilitation exoskeleton robot," *Applied Sciences (Switzerland)*, vol. 10, no. 7, 2020.
- [20] M. Sharifi, J. K. Mehr, V. K. Mushahwar, and M. Tavakoli, "Adaptive cpg-based gait planning with learning-based torque estimation and control for exoskeletons," *IEEE Robotics and Automation Letters*, vol. 6, no. 4, pp. 8261–8268, 2021.
- [21] H. Kazerooni, R. Steger, and L. Huang, "Hybrid control of the Berkeley Lower Extremity Exoskeleton (BLEEX)," *International Journal of Robotics Research*, vol. 25, no. 5-6, pp. 561–573, 2006.
- [22] J. C. Moreno, N. Vitiello, C. Walsh, H. Huang, and S. Mohammed, "Introduction to the special section on wearable robots," *IEEE Transactions on Robotics*, vol. 38, no. 3, pp. 1338–1342, 2022.
- [23] R. M. Andrade and P. Bonato, "The Role Played by Mass, Friction, and Inertia on the Driving Torques of Lower-Limb Gait Training Exoskeletons," *IEEE Transactions on Medical Robotics and Bionics*, vol. 3, no. 1, pp. 125–136, 2021.
- [24] D. Zanotto, T. Lenzi, P. Stegall, and S. K. Agrawal, "Improving transparency of powered exoskeletons using force/torque sensors on the supporting cuffs," in *2013 IEEE 13th International Conference on Rehabilitation Robotics (ICORR)*, 2013, pp. 1–6.
- [25] W. van Dijk, H. van der Kooij, B. Koopman, E. H. F. van Asseldonk, and H. van der Kooij, "Improving the transparency of a rehabilitation robot by exploiting the cyclic behaviour of walking," in *2013 IEEE 13th International Conference on Rehabilitation Robotics (ICORR)*, 2013, pp. 1–8.
- [26] J. Pratt, P. Dilworth, and G. Pratt, "Virtual model control of a bipedal walking robot," in *Proceedings of International Conference on Robotics and Automation*, vol. 1, 1997, pp. 193–198 vol.1.
- [27] M. Mistry, J. Buchli, and S. Schaal, "Inverse dynamics control of floating base systems using orthogonal decomposition," in *2010 IEEE International Conference on Robotics and Automation*, 2010, pp. 3406–3412.
- [28] J. Vantilt, C. Giraddi, E. Aertbeliën, F. De Groote, and J. De Schutter, "Estimating contact forces and moments for walking robots and exoskeletons using complementary energy methods," *IEEE Robotics and Automation Letters*, vol. 3, no. 4, pp. 3410–3417, 2018.
- [29] M. J. Claros, R. Soto, J. L. Gordillo, J. L. Pons, and J. L. Contreras-Vidal, "Robotic assistance of human motion using active-backdrivability on a geared electromagnetic motor," *International Journal of Advanced Robotic Systems*, vol. 13, no. 2, pp. 1–10, 2016.
- [30] J. Fong, E. B. Küçüktabak, V. Crocher, Y. Tan, K. Lynch, J. Pons, and D. Oetomo, "CANopen Robot Controller (CORC): An open software stack for human robot interaction development," *The International Symposium on Wearable Robotics (WeRob2020)*, vol. 2020, pp. –ss, 2020.
- [31] L. Li, Z. Xie, X. Luo, and J. Li, "Effects of torso pitch motion on energy efficiency of biped robot walking," *Applied Sciences*, vol. 11, no. 5, 2021.
- [32] B. Hwang and D. Jeon, "A method to accurately estimate the muscular torques of human wearing exoskeletons by Torque sensors," *Sensors (Switzerland)*, vol. 15, no. 4, pp. 8337–8357, 2015.
- [33] M. Fumagalli and R. Carloni, "A modified impedance control for physical interaction of UAVs," *IEEE International Conference on Intelligent Robots and Systems*, pp. 1979–1984, 2013.
- [34] Y. Zimmermann, E. B. Kucuktabak, F. Farshidian, R. Riener, and M. Hutter, "Towards Dynamic Transparency : Robust Interaction Force Tracking Using Multi-Sensory Control on an Arm Exoskeleton," *IEEE/RSJ International Conference on Intelligent Robots and Systems (IROS)*, pp. 7417–7424, 2020.
- [35] B. Stellato, G. Banjac, P. Goulart, A. Bemporad, and S. Boyd, "OSQP: an operator splitting solver for quadratic programs," *Mathematical Programming Computation*, vol. 12, no. 4, pp. 637–672, 2020.
- [36] C. Dario Bellicoso, C. Gehring, J. Hwangbo, P. Fankhauser, and M. Hutter, "Perception-less terrain adaptation through whole body control and hierarchical optimization," *IEEE-RAS International Conference on Humanoid Robots*, pp. 558–564, 2016.
- [37] Y. Zimmermann, A. Forino, R. Riener, and M. Hutter, "ANYexo: A Versatile and Dynamic Upper-Limb Rehabilitation Robot," *IEEE Robotics and Automation Letters*, vol. 4, no. 4, pp. 3649–3656, 2019.
- [38] M. K. MacLean and D. P. Ferris, "Human muscle activity and lower limb biomechanics of overground walking at varying levels of simulated reduced gravity and gait speeds," *PLoS ONE*, vol. 16, no. 7 July, pp. 1–23, 2021.
- [39] Y. Wen, J. Si, A. Brandt, X. Gao, and H. H. Huang, "Online reinforcement learning control for the personalization of a robotic knee prosthesis," *IEEE Transactions on Cybernetics*, vol. 50, no. 6, pp. 2346–2356, 2020.
- [40] E. B. Küçüktabak, S. J. Kim, Y. Wen, K. Lynch, and J. L. Pons, "Human-machine-human interaction in motor control and rehabilitation: a review," *Journal of NeuroEngineering and Rehabilitation*, vol. 18, no. 1, p. 183, Dec 2021.
- [41] S. J. Kim, Y. Wen, E. B. Küçüktabak, S. Zhan, K. Lynch, L. Hargrove, E. J. Perreault, and J. L. Pons, "A framework for dyadic physical interaction studies during ankle motor tasks," *IEEE Robotics and Automation Letters*, vol. 6, no. 4, pp. 6876–6883, 2021.
- [42] S. J. Kim, Y. Wen, D. Ludvig, E. B. Küçüktabak, M. R. Short, K. Lynch, L. Hargrove, E. J. Perreault, and J. L. Pons, "Effect of dyadic haptic collaboration on ankle motor learning and task performance," *IEEE Transactions on Neural Systems and Rehabilitation Engineering*, pp. 1–1, 2022.